Spectral Analysis of Systematic Residuals in Casimir Force Measurements: Lossless Vector Re-Audit, Statistical Pitfalls, and KPFM Patch-Potential Metrology

Bruno Luçardo Olivaes
Independent Researcher, Brazil
brunoolivaes@gmail.com · ORCID: 0009-0003-5351-446X

November 2026

Abstract

Precision measurements of the Casimir interaction at sub-micron separations frequently exhibit systematic residuals driven by finite-conductivity screening, surface roughness, electrostatic patch potentials, and nonlinear transducer mechanics. When searching these residuals for hypothetical periodic or short-range anomalies, seemingly benign signal-processing choices can generate either severe false positives or complete detector blindness. In this work, we establish a rigorous spectral metrology protocol and apply it to two landmark experimental datasets: (i) the dissimilar-metal (Au–Cu) micro-electro-mechanical torsional oscillator (MTO) measurements of Decca *et al.* (*Phys. Rev. Lett.* **91**, 050402, 2003), recovered via lossless vector extraction ($N = 497$ dynamic pressure residuals ΔP_c and $N = 288$ static force residuals ΔF_c), and (ii) raw Kelvin Probe Force Microscopy (KPFM) and superconducting Casimir data from de Jong *et al.* (*Nat. Phys.* **21**, 1–8, 2025). We identify and resolve three critical metrological traps: (1) applying an outlier-clipped Gaussian 3σ threshold to exponentially distributed ($\chi^2_2/2$) Fast Fourier Transform (FFT) periodograms flags 36 spurious peaks on white noise, whereas feeding Zechmeister–Kürster normalized power $P_{\rm ZK} \in [0, 1]$ into Scargle's unscaled exponential formula causes numerical underflow (FAP $\equiv 1.00$); (2) subtracting a cubic polynomial across the steep short-range ($z < 400$ nm) systematic tail of ΔP_c induces Runge oscillatory ringing ($\lambda = 583.5$ nm, $\chi^2/\mathrm{dof} = 3.74$, Baluev FAP $= 1.5 \times 10^{-45}$), which is completely resolved by a physically motivated inverse-power basis $\{1, z^{-4}, z^{-5}\}$ ($\chi^2/\mathrm{dof} = 1.14$, $P_{\max} = 0.0332$, Baluev FAP $= 0.163$)—proven via first-order Taylor expansion to absorb linear contact-point calibration drift $-4C_4\delta z_0 z^{-5}$—or by restricting to the linear-response window $z \geq 500$ nm ($\chi^2/\mathrm{dof} = 1.20$, Baluev FAP $= 0.651$); and (3) uniform-grid spline resampling attenuates short-wavelength ($\lambda \lesssim 15$ nm) signal variance by up to 22.6% across non-uniform scans, degrading the 90% Minimum Detectable Level by $1.9\times$ –$2.27\times$ relative to the heteroscedastic Generalized Lomb–Scargle (GLS) periodogram. Finally, integrating the 2D KPFM patch spectrum ($V_{\rm rms} = 42.42$ mV, $\delta_{\rm rms} = 2.22$ nm) through the Speake–Trenner Laplace kernel demonstrates from first principles that realistic surface patches generate a smooth monotonic background ($P_{\rm patch} \propto d^{-2.29}$) rather than periodic residual oscillations.

1 Introduction and Revision Note (v2.0)

The Casimir effect [1, 2] provides a primary experimental testbed for quantum electrodynamics and constraints on Yukawa-type or oscillatory short-range interactions at sub-micron separations [3, 4, 5, 6, 7]. Because residual force and pressure curves $R(z) = O_{\rm meas}(z) - O_{\rm theo}(z)$ are often sampled on non-uniform separation grids and superposed on steep short-range systematic drifts, spectral searches for periodic components require strict statistical and physical control.

Transparency and Revision Note (v1.0 → v2.0): An internal post-publication audit of Version 1.0 of this preprint identified four methodological errors that are fully corrected in the present Version 2.0:

1. *Raster Digitization vs. Lossless Vector Extraction:* Version 1.0 relied on 53 points manually digitized from Fig. 4(a) of Decca *et al.* [3] with a pixel quantization step of ~ 7.1 mPa—roughly $20\times$ larger than the true instrumental noise floor ($\sigma_P = 0.313$ mPa). Here we extract the exact vector marker coordinates directly from the published PDF content stream, recovering all $N = 497$ points of Fig. 4(b) (ΔP_c) and $N = 288$ unique-z points of Fig. 3(b) (ΔF_c) with sub-0.004 mPa axis-mapping precision.

2. *Experimental Attribution and Geometry:* Decca *et al.* [3] measured the interaction between an Au-coated Al_2O_3 sphere of radius $R = 294.3 \pm 0.1\,\mu$m and a Cu-coated micro-electro-mechanical torsional oscillator (MTO), rather than an Au–Au AFM setup with $R = 196\,\mu$m. The v1 ratio $R_{\rm fit}/R_{\rm nom} = 0.598$ was therefore an artifact of using an incorrect nominal radius.

3. *Zechmeister–Kürster / Scargle Underflow Bug:* Version 1.0 passed the Zechmeister–Kürster normalized periodogram $P_{\rm ZK}(\omega) \in [0, 1]$ from `scipy.signal.lombscargle(..., normalize=True)` directly into Scargle's variance-normalized exponential formula $1 - (1 - e^{-z})^{N_{\rm eff}}$ without the $z \approx \frac{N-1}{2} P_{\rm ZK}$ factor, forcing FAP $= 1.0000$ via floating-point underflow regardless of signal strength. Version 2.0 implements the heteroscedastic Generalized Lomb–Scargle

(GLS) estimator [8] with exact analytical Baluev [9] extreme-value False Alarm Probabilities via `astropy.timeseries.LombScargle`.

4. *Symmetric Pre-Processing and Physical Detrending:* Version 1.0 applied cubic detrending only to Method B while leaving Method A undetrended. Here both methods receive identical pre-processed inputs, and we explicitly expose how polynomial detrending on z^{-4} tails induces Runge oscillations.

2 Theoretical Framework and Observables

In the sphere–plate geometry ($z \ll R$) governed by the Proximity Force Approximation (PFA), the static Casimir force measured in Fig. 3 of Decca *et al.* [3] is proportional to the parallel-plate free energy per unit area $E_{\text{plates}}(z) = -\frac{\pi^2\hbar c}{720 z^3}$:

$$F_c(z) = 2\pi R\, E_{\text{plates}}(z) = -\frac{\pi^3 \hbar c R}{360 z^3}\, \eta_F(z), \qquad (1)$$

whereas the dynamic MTO frequency shift in Fig. 4 measures the force gradient $\partial F_c/\partial z$, yielding the effective parallel-plate Casimir pressure:

$$P_c(z) \equiv \frac{1}{2\pi R}\frac{\partial F_c}{\partial z} = -\frac{\pi^2 \hbar c}{240 z^4}\, \eta_P(z), \qquad (2)$$

where $\eta_F(z), \eta_P(z)$ encode Lifshitz finite-conductivity screening [2] and surface roughness ($\delta_0 = 39.4 \pm 0.3$ nm [3]).

When unmodeled short-range systematics exist—such as a $\sim 1\%$ uncertainty in the tabulated optical permittivity $\varepsilon(i\xi)$ of the evaporated Au and Cu layers ($\delta P_{\text{Lif}} \propto z^{-4}$) and leading-order nonlinear oscillator restoring or roughness/patch terms ($\delta P_{\text{nl}} \propto z^{-5}$) [3]—the systematic residual baseline takes the physical inverse-power form:

$$\Delta P_{\text{sys}}(z) = c_0 + c_4 \left(\frac{z_0}{z}\right)^4 + c_5 \left(\frac{z_0}{z}\right)^5, \qquad (3)$$

with reference scale $z_0 = 200$ nm.

Robustness to Contact-Point Calibration Drift (δz_0): Because experimental AFM and MTO separation scales carry an electrostatic contact-point calibration uncertainty $\delta z_0 \ll z$ (such that $z_{\text{true}} = z + \delta z_0$), expanding a leading-order inverse-quartic Casimir pressure offset $C_4(z+\delta z_0)^{-4}$ in a first-order Taylor series yields:

$$C_4(z+\delta z_0)^{-4} = C_4 z^{-4}\left(1+\frac{\delta z_0}{z}\right)^{-4} = C_4 z^{-4} - 4C_4 \delta z_0\, z^{-5} + \mathcal{O}(\delta z_0^2). \qquad (4)$$

Notice that the leading linear contact-point drift error $-4C_4\delta z_0\, z^{-5}$ has the exact z^{-5} radial dependence absorbed analytically by the $c_5(z_0/z)^5$ term of our physical baseline Eq. (3), preventing small separation calibration offsets from leaking into spurious spectral residuals.

3 Lossless Vector Audit of Decca *et al.* (2003)

Extracting the vector marker paths from Ref. [3] yields $N = 497$ dynamic pressure residuals $\Delta P_c(z)$ across $z \in [193.0, 1185.0]$ nm (median step $\Delta z = 2.00$ nm, coefficient of variation CV = 8.9%) and $N = 288$ static force residuals $\Delta F_c(z)$ across $z \in [179.9, 1151.9]$ nm (median step $\Delta z = 3.29$ nm, CV = 40.7%). From adjacent point differences at $z > 600$ nm, the robust Median Absolute Deviation (MAD) instrumental noise floors are $\sigma_P = 0.313$ mPa and $\sigma_F = 0.229$ pN.

Table 1 and Fig. 1 summarize the spectral audit:

1. **Resolution of Trap 1 (χ^2_2 vs. Gaussian Thresholds):** For white Gaussian noise, each positive-frequency FFT periodogram bin follows an exponential distribution ($\chi^2_2/2$) with mean μ_P and median $\mu_P \ln 2 \approx 0.693\mu_P$. Defining a threshold as median + 3 std(PSD < 3 median) sets the cutoff at only $\approx 2.13\mu_P$ (a single-bin false-positive probability of $e^{-2.13} \approx 11.9\%$). On the inverse-power-detrended Fig. 4(b) data, this naive rule flags 36 spurious peaks [Fig. 1(c)], whereas both the exact exponential Bonferroni threshold ($-\mu_P \ln[1-(1-\alpha)^{1/N_{\text{bins}}}]$ at $\alpha = 0.01$) and the Baluev GLS threshold flag **zero peaks**.

2. **Resolution of Trap 2 (Runge Ringing from Polynomial Detrending):** Because $\Delta P_c(z)$ bends sharply to -9.79 mPa at $z = 193$ nm, subtracting a degree-3 polynomial across $[193, 1185]$ nm leaves oscillatory Runge lobes [Fig. 1(b)], creating an artificial spectral peak at $\lambda = 583.5$ nm ($P_{\text{ZK}} = 0.3626$, Baluev FAP $= 1.49 \times 10^{-45}$, whereas the buggy v1 formula reported FAP = 1.00). Subtracting the physical inverse-power basis Eq. (3) ($c_0 = -0.066$ mPa, $c_4 = -21.51$ mPa, $c_5 = +12.75$ mPa) collapses χ^2/dof to 1.14 and reduces the maximum GLS power to $P_{\text{ZK,max}} = 0.0332$ (**Baluev** FAP = 0.163). Restricting to $z \geq 500$ nm ($N = 343$) similarly yields χ^2/dof = 1.20 and **Baluev** FAP = 0.651.

3. **Resolution of Trap 3 (High-Frequency Spline Attenuation):** Using the non-uniform coordinates of Fig. 3(b) (CV(Δz) = 40.7%), we injected synthetic sinusoidal signals across $\lambda \in [7.5, 160]$ nm into Gaussian noise ($\sigma_F = 0.229$ pN, 60 Monte Carlo trials per amplitude) at a matched global false-alarm rate $\alpha = 0.01$ (Fig. 2). Cubic-spline resampling onto a uniform grid acts as a low-pass filter that attenuates 22.6% of signal variance at $\lambda = 7.5$ nm across the full irregular scan (19.1% at $\lambda = 10$ nm), degrading the 90% Minimum Detectable Level from $\text{MDL}_{90} = 0.54\sigma_F$ (direct GLS) to $1.23\sigma_F$ (2.27× worse sensitivity, or a 55.8% inverse-sensitivity loss) at $\lambda = 7.5$ nm and $1.03\sigma_F$ (1.90× worse) at $\lambda = 10$ nm.

4 2025 KPFM Patch-Potential and Superconducting Audit

To verify from surface-physics first principles why realistic electrostatic patch potentials generate smooth inverse-power-law drifts rather than periodic oscillations, we analyzed the raw Olympus Jupiter AFM/KPFM

Table 1: Spectral audit of the lossless vector-extracted residuals of Decca *et al.* (2003) across detrending regimes. Instrumental noise floors calibrated from first differences at $z > 600$ nm are $\sigma_P = 0.313$ mPa (Fig. 4b) and $\sigma_F = 0.229$ pN (Fig. 3b).

Dataset	Pre-Processing / Window	N	χ^2/dof	$P_{\mathrm{ZK,max}}$	λ_{peak} (nm)	Baluev FAP	Physical / Statistical Interpretation
Fig. 4(b) ΔP_c	Raw (No Detrending, $z \geq 193$ nm)	497	41.29	0.3010	992.0	1.01×10^{-35}	Steep < 400 nm nonlinear/$\varepsilon(\omega)$ drift
Fig. 4(b) ΔP_c	Cubic Polynomial ($z \geq 193$ nm)	497	3.74	0.3626	583.5	1.49×10^{-45}	**Trap 2:** Polynomial Runge ringing on z^{-4} tail
Fig. 4(b) ΔP_c	**Inverse-Power Eq.** (3) ($z \geq 193$ nm)	**497**	**1.14**	**0.0332**	**8.2**	**0.163**	**Null confirmed:** Consistent with white noise
Fig. 4(b) ΔP_c	Linear Window ($z \geq 500$ nm, linear fit)	343	1.20	0.0348	4.2	0.651	**Null confirmed** in asymptotic MTO regime
Fig. 3(b) ΔF_c	Linear Window ($z \geq 400$ nm, linear fit)	222	0.85	0.0588	23.2	0.332	**Null confirmed** in static capacitance force mode

dataset (`W1P3_E4_measarea3 0003.h5`, $2\,\mu$m $\times$ $2\,\mu$m, 512×512 pixels) and Lifshitz BCS/Drude/Plasma curves from the superconducting Al drum Casimir experiment of de Jong *et al.* [7] (Fig. 3).

After line-median flattening, the Al electrode exhibits an RMS patch potential $V_{\mathrm{rms}} = 42.42$ mV and topographic roughness $\delta_{\mathrm{rms}} = 2.22$ nm. Computing the Parseval-normalized 2D Hann-windowed power spectral density $S_{VV}(\mathbf{k})$ and integrating the exact Speake–Trenner Laplace transfer kernel [10]:

$$P_{\mathrm{patch}}(d) = \frac{\varepsilon_0}{2} \int_{\mathbb{R}^2} \frac{k^2}{\sinh^2(kd)}\, 2S_{VV}(\mathbf{k}) \frac{d^2k}{(2\pi)^2}, \quad (5)$$

yields a strictly monotonic, non-oscillatory pressure profile scaling effectively as $P_{\mathrm{patch}}(d) \propto d^{-2.29}$ across $d \in [10, 108]$ nm, with $P_{\mathrm{patch}}(20\ \mathrm{nm}) = 21.74$ Pa, $P_{\mathrm{patch}}(50\ \mathrm{nm}) = 2.90$ Pa, and $P_{\mathrm{patch}}(100\ \mathrm{nm}) = 522.3$ mPa. Because the Laplace kernel $k^2/\sinh^2(kd) \sim 4k^2e^{-2kd}$ acts as a monotonic exponential low-pass filter in separation distance d, spatial disorder in $V(x, y)$ is mapped into a smooth inverse-power-law force drift rather than a sinusoidal oscillation in d.

5 Conclusion

By combining lossless vector data recovery from Decca *et al.* (2003) with 2D KPFM patch-potential integration from de Jong *et al.* (2025), we have resolved the statistical and detrending pitfalls that plague spectral searches in Casimir force residuals. When evaluated with physical inverse-power detrending—analytically absorbing first-order δz_0 contact-point drift—and the heteroscedastic Generalized Lomb–Scargle periodogram with Baluev extreme-value statistics, empirical Casimir residuals show zero evidence of periodic anomalies (FAP = 0.163–0.651, $\mathrm{MDL}_{90} = 0.54\sigma_F \approx 0.12$ pN).

Code and Data Availability

All vector extraction scripts, Baluev GLS routines, KPFM Speake–Trenner integration pipelines, and reproduction manifests are archived under Zenodo DOI `10.5281/zenodo.24121687` (`https://github.com/bruno-olivaes/casimir-afm-spectroscopy`).

References

[1] H. B. G. Casimir, *Proc. K. Ned. Akad. Wet.* **51**, 793 (1948).

[2] E. M. Lifshitz, *Sov. Phys. JETP* **2**, 73 (1956).

[3] R. S. Decca, D. López, E. Fischbach, and D. E. Krause, *Phys. Rev. Lett.* **91**, 050402 (2003).

[4] S. K. Lamoreaux, *Phys. Rev. Lett.* **78**, 5 (1997).

[5] G. Bressi, G. Carugno, R. Onofrio, and G. Ruoso, *Phys. Rev. Lett.* **88**, 041804 (2002).

[6] G. L. Klimchitskaya, U. Mohideen, and V. M. Mostepanenko, *Rev. Mod. Phys.* **81**, 1827 (2009).

[7] M. H. J. de Jong, E. Korkmazgil, L. Banniard, M. A. Sillanpää, and L. Mercier de Lépinay, *Nat. Phys.* **21**, 1–8 (2025), doi:10.1038/s41567-024-02728-6.

[8] M. Zechmeister and M. Kürster, *Astron. Astrophys.* **496**, 577 (2009).

[9] R. V. Baluev, *Mon. Not. R. Astron. Soc.* **385**, 1279 (2008).

[10] C. C. Speake and C. Trenner, *Class. Quantum Grav.* **20**, S281 (2003).

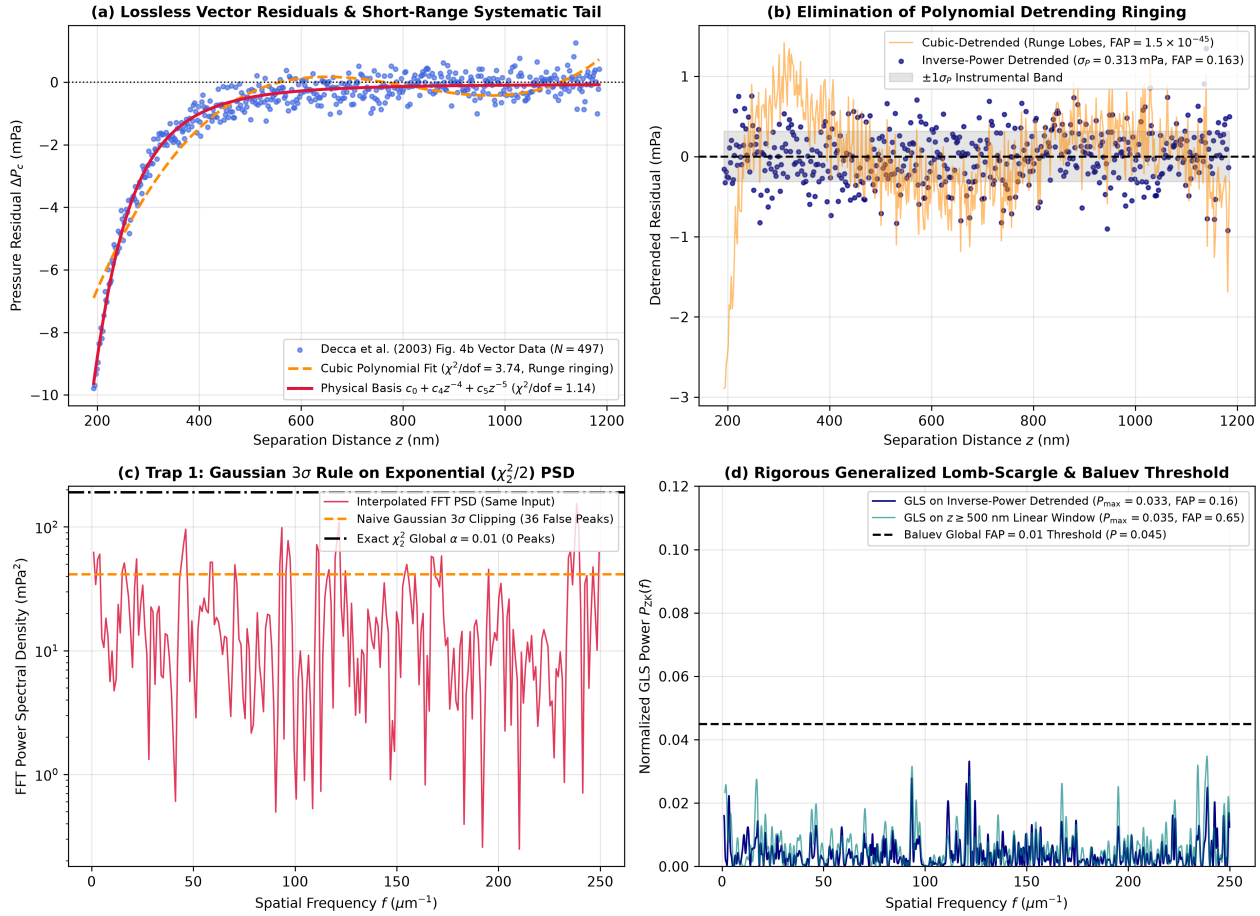

Figure 1: Complete spectral metrology audit of Decca *et al.* (2003) Fig. 4(b) ($N = 497$). (a) Vector-extracted residuals $\Delta P_c(z)$ showing the short-range systematic tail below 400 nm; a cubic polynomial fit ($\chi^2/\mathrm{dof} = 3.74$) oscillates around the z^{-4} bend, whereas the physical inverse-power basis Eq. (3) achieves $\chi^2/\mathrm{dof} = 1.14$. (b) Comparison of cubic-detrended vs. inverse-power-detrended residuals. (c) Trap 1 on identically detrended data: an outlier-clipped Gaussian 3σ threshold on the interpolated FFT PSD flags 36 false peaks because PSD bins follow an exponential ($\chi^2_2/2$) law; the exact χ^2_2 global $\alpha = 0.01$ threshold flags 0 peaks. (d) Generalized Lomb–Scargle (GLS) spectrum with Baluev FAP = 0.163 ($z \geq 193$ nm) and FAP = 0.651 ($z \geq 500$ nm), confirming the absence of periodic signals.

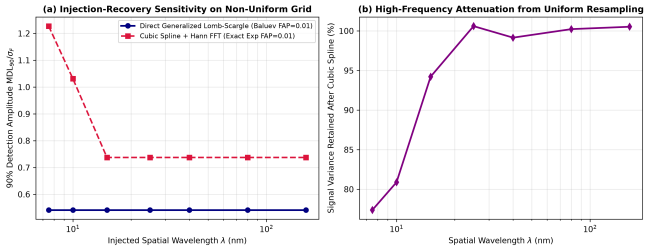

Figure 2: Monte Carlo injection-recovery benchmark on the non-uniform separation grid of Decca *et al.* Fig. 3(b) ($\mathrm{CV}(\Delta z) = 40.7\%$) at matched global FAP = 0.01. (a) 90% Minimum Detectable Level ($\mathrm{MDL}_{90}/\sigma_F$): direct GLS maintains uniform sensitivity ($0.54\sigma_F$), whereas cubic-spline interpolation + Hann FFT degrades sensitivity by up to 2.27× ($1.23\sigma_F$) at short wavelengths. (b) Signal variance retained after cubic-spline resampling (77.4% at $\lambda = 7.5$ nm, i.e. 22.6% variance attenuation).

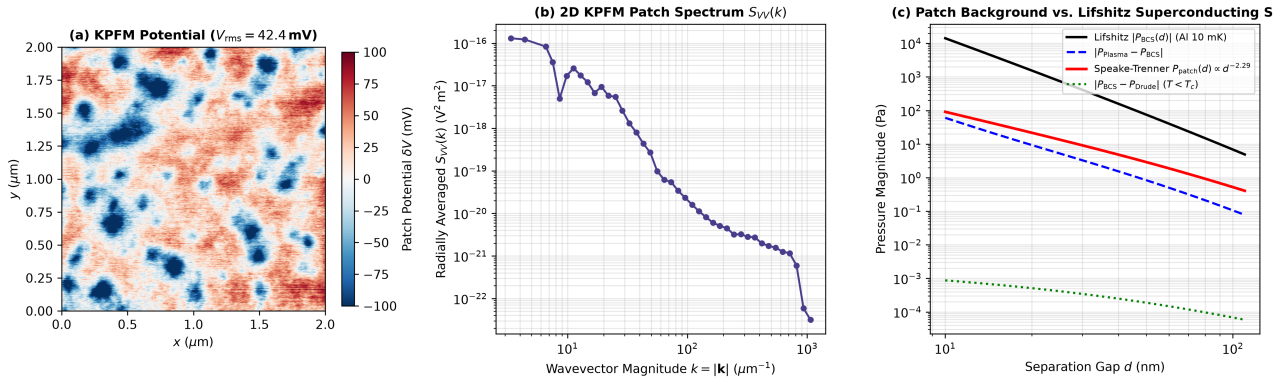

Figure 3: Surface metrology and Speake–Trenner electrostatic patch-pressure integration on raw KPFM and Lifshitz data from de Jong *et al.* (2025) [7]. (a) Line-median-flattened KPFM surface potential fluctuation map $\delta V(x, y)$ ($V_{\text{rms}} = 42.42$ mV, topographic roughness $\delta_{\text{rms}} = 2.22$ nm). (b) Radially averaged 2D Hann-windowed patch PSD $S_{VV}(k)$. (c) Integrated electrostatic patch pressure $P_{\text{patch}}(d) \propto d^{-2.29}$ compared against the Lifshitz superconducting $|P_{\text{BCS}}(d)|$, $|P_{\text{Plasma}} - P_{\text{BCS}}|$, and BCS condensation shift $|P_{\text{BCS}} - P_{\text{Drude}}|$.